Rare earth elements in apatite: A proxy for unravelling carbonatite melt compositions

Haihao Guo, Johann Tuduri, Zineb Nabyl, Saskia Erdmann, Xiaochun Li, Fabrice Gaillard

Rare Earth Elements in apatite: a proxy for unravelling carbonatite melt compositions

Haihao Guo[1,2], Johann Tuduri[1], Zineb Nabyl[3], Saskia Erdmann[1], Xiaochun Li[4], Fabrice Gaillard[1]

[1] Univ. Orléans, CNRS, BRGM, ISTO, UMR 7327, F-45071, Orléans, France

[2] State Key Laboratory of Geological Processes and Mineral Resources, School of Earth Sciences, China University of Geosciences, Wuhan 430074, China

[3] CEA, DES, ISEC, DE2D, University of Montpellier, Marcoule, France

[4] Key Laboratory of Mineral Resources, Institute of Geology and Geophysics, Chinese Academy of Sciences, Beijing 100029, China

Abstract

Carbonatites are fascinating magmatic rocks because of their anomalous compositions, including the fact that some of these rocks host major rare earth element (REE) deposits. Despite much recent work, our understanding of their genesis and the composition of initial carbonatite melts is hindered by two major obstacles: most carbonatites we see are intrusive rocks, and they are commonly affected by metasomatic overprint. Here, we report experimental data in which we use apatite as a geochemical proxy to see back through crystallization and metasomatic events, thus making it possible to decipher the composition of carbonatite melts. We determined partition coefficients between apatite and carbonatite melts for a broad range of elements. The Na-rich nature of carbonatite melts plays an important role in apatite-melt partition coefficients, which are in the range of 1-7 for Sr, Y and REE in carbonatite systems. Using our new experimental data combined with >700 apatite composition data from carbonatites in various geodynamic settings, we show that carbonatite melt REE contents vary by more than two orders of magnitude. This variation cannot be solely produced by crystal-melt fractionation, implying that some carbonatite melts must be REE-rich or REE-poor initially, and that they mostly remain so during differentiation. We conclude that the degree of REE enrichment reflects carbonatite melts produced by immiscibility from variably differentiated alkaline magmas.

1. Introduction

Intrusive carbonatite complexes are rare magmatic rocks that occur in the Earth's crust, which have attracted much attention within the geochemical community. The reason for this particular interest is that carbonatites display several enigmatic geochemical features: (i) in contrast to the majority of magmas, they are silica-depleted (Massuyeau et al., 2020) and contains > 20 wt% CO_2, implying a strong link with the carbon geodynamic cycle (Dasugpta, 2013); (ii) they are inferred to be rich in water, sulfur and halogens (Keppler, 2003; de Moor et al., 2013); (iii) they can be strongly enriched in REE and other rare metals, e.g., Nb, Ta, Zr, Th and U, and as a result, the global source for certain critical metals resides in a few exposed carbonatites (Verplanck et al., 2016). The unusual nature of carbonatites thus constitutes a geochemical anomaly, with both environmental and societal importance. In spite of their importance and numerous studies addressing the genesis and evolution of carbonatites, the mode of formation of these rocks remains elusive. It has long been proposed that carbonatites may be produced by (i) partial melting of a carbonated mantle (Sweeney, 1994; Foley et al., 2009); (ii) fractional crystallization of carbonated silicate magma (Lee and Wyllie, 1994; Veksler et al., 1998) and/or (iii) liquid immiscibility (Halama et al., 2005; Mitchell, 2009; Gittins and Mitchell, 2023). Is there a way to relate these general types of formation to the enigmatic geochemical features identified above? In particular, why do only few carbonatites contain economically-viable REE concentrations whereas others contain much less REE (Fig. 1)? The latter question is critical for improving our understanding of carbonatite genesis and REE ore deposit formation, and provides the core motivation for numerous recent studies (Yaxley et al., 2022 and the reference therein).

Carbonatite rocks contain substantial volatiles (e.g., F, Cl and S), as abundant apatite ($Ca_5(PO_4)_3(OH, Cl, F)$), fluorite (CaF_2), barite ($BaSO_4$), carbonate (various minerals with compositions $(Ca,Mg,Fe)CO_3$) and sulphide minerals (Le Bas, 1989; McLemore, 2018). The REE contents of carbonatites can be high, but are above all strikingly variable (Smith et al., 2016), ranging from hundred ppm to several weight%, as shown by the REE contents of more than 3500 natural carbonatite rocks from the GEOROC database (Fig. 1, http://georoc.mpch-mainz.gwdg.de/georoc/). Establishing links between these geochemical features has been difficult since almost all exposed carbonatites are intrusions, consisting mainly of calcite or dolomite cumulates, which

certainly differ from the composition of their parental magmas (Xu et al., 2007; Weidendorfer et al., 2017; Yaxley et al., 2022). Moreover, carbonatite rocks have commonly experienced metasomatic processes, which can drastically change their volatile element content and REE distribution (Le Bas, 1989; Anenburg et al., 2020). As a consequence, our knowledge of the composition of carbonatite melts remains poor, making it difficult to discriminate carbonatite rocks that preserve a magmatic signature from those affected by hydrothermal processes.

Despite limited information regarding the precise composition and liquid line of descent of carbonatite melts derived from the mantle, recent advancements have informed our working hypotheses, such as studies on extrusive carbonatite rocks, carbonatite melt inclusions and experimental petrology. (1) The unique occurrence of extrusive carbonatites at Oldonyo Lengai, Tanzania, reveals Na-rich melt compositions that differ from the majority of intrusive carbonatites and are highly differentiated carbonatites (Weidendorfer et al., 2017). These extrusive rocks are, however, unlikely to represent a universal proxy of carbonatite melts (De Moor et al., 2013; Gusmicz et al., 2019; Berkesi et al., 2020; Yaxley et al., 2022). (2) The study of melt inclusions is a powerful tool for determining initial melt compositions, and existing data point towards Na-rich compositions (Guzmics et al., 2012; 2015; 2019). Nevertheless, carbonatite melt inclusions are very scarce and their chemical compositions are difficult to quantify due to post-entrapment processes and the fact that, in most cases, carbonate and silicate melt inclusions are associated (Yaxley et al., 2022). (3) Experimental petrology has been used to link Na-rich melts and the Ca-rich nature of intrusive carbonatites (Weidendorfer et al., 2018), clearly demonstrating that all carbonatite melts must contain a significant amount of Na. Yet, many unanswered questions remain regarding the mechanisms underlying the wide range of REE found in carbonatite rocks that crystallize from Na-rich and volatile-rich carbonatite systems (Anenburg et al., 2021). In particular, possible links between REE abundance in carbonatite melts and different genetic models for carbonatite melt generation remain highly debated.

We propose here to investigate the volatile and REE contents in carbonatite melts by means of a suitable proxy mineral. Apatite is the obvious mineral, because it is commonly found in carbonatite rocks (Chakhmouradian et al., 2017), and can incorporate all of the major magmatic volatile species (F, S, Cl), as well as REE, into its structure (Pan and Fleet, 2002). Knowledge of the partition coefficients between

apatite and carbonatite melt makes it possible to decipher the elusive geochemical record of the early magmatic carbonatite history. There are three representative experimental studies on the partitioning of trace elements between apatite and carbonatite melts (Klemme and Dalpé, 2003; Hammouda et al., 2010; Sartori et al., 2023), but the results for REE are not consistent. Klemme and Dalpé (2003) found REE to be incompatible in apatite, with partition coefficients of less than 1 at 1 GPa and 1250 °C, whereas Hammouda et al. (2010) and Satorti et al., (2023) found them to be compatible in apatite at 4-6 GPa and 1200-1380 °C. Besides, two studies used dry calcite melts as the starting material at mantle conditions (Klemme and Dalpé, 2003; Hammouda et al., 2010), whereas carbonatite magmas must contain significant amounts of alkali and volatile elements (Guzmics et al., 2019; Weidendorfer et al., 2017; Berkesi et al., 2020).

Here, we present new experiments defining partition coefficients between apatite and an alkali-rich carbonatite melt (Table 1) with various volatile element (H, F, S, Cl) concentrations. The experiments were performed at 800 °C, 200 MPa and over a range of oxygen fugacities (log fO_2 ranges from ~ Δ FMQ + 0 to Δ FMQ + 3; FMQ – fayalite-magnetite-quartz buffer) using internally heated pressure vessels, IHPV (Table 2). We also determined the apatite-melt partition coefficients for the piston cylinder (PC) experiments of Nabyl et al. (2021), which were conducted over a broader range of conditions from 850 to 1050 °C and at 800 MPa (Table 2). We found that the apatite-melt REE partition coefficients in geologically realistic carbonatite melt compositions vary within a narrow range, with values of 1-7. This implies that individual REE partitioning between apatite and carbonatite melt are independent on pressure, temperature and volatile activities. These new results are used to quantify the REE abundances for natural carbonatite melts using apatite as a proxy. The calculated REE abundances for carbonatite melts greatly vary, encompassing a range of concentration consistent with the genesis of most carbonatite rocks by immiscibility with alkaline melts.

2. Methods

2.1. Anhydrous starting materials

Several starting materials were investigated in this study (Table 1). The starting materials used for the IHPV and PC experiments were prepared by mixing synthetic carbonates, oxides, silicates and apatite, following the procedure of Nabyl et al. (2021). The carbonatite powder was prepared from a mixture of high-purity synthetic powders (SiO_2, TiO_2, Al_2O_3, Fe_2O_3, MnO_2, $CaCO_3$, Na_2CO_3, K_2CO_3, $SrCO_3$, and $BaCO_3$) and natural magnesite ($MgCO_3$). The bulk compositions of the starting carbonatite powders are given in Table 1. The starting carbonatite materials were then doped with REE and other trace elements in the form of oxides or fluorides (La_2O_3, CeO_2, Pr_6O_{11}, Nd_2O_3, Sm_2O_3, Eu_2O_3, Gd_2O_3, Tb_4O_7, Dy_2O_3, Ho_2O_3, Er_2O_3, Yb_2O_3, Lu_2O_3, Sc_2O_3, Y_2O_3, Nb_2O_5, Ta_2O_5, ZrO_2, HfO_2, PbO, NiO, CoO, MoO_3 and WO_3). The powders were first mixed in an agate mortar by hand (for ~30 minutes) in a glove box to avoid atmospheric water contamination, and then by an automatic grinder with an agate mortar and ball mill (for ~30 minutes). For F-, Cl- and S-doped experiments in IHPV, NaF, NaCl and Na_2SO_4 powders were further added to the starting carbonatite for IHPV runs (Table 1). For experiments in PC, the staring carbonatite runs were directly doped with phonolite and P_2O_5 powders (Table 2) as described in Nabyl et al. (2021). Prior to and between all experiments, the synthetic powders were stored in a dry oven at 120 °C.

2.2.Sample preparation

Sample preparation for IHPV and PC experiments followed the same protocol. The starting material powders were taken out of the 120 °C oven directly prior to loading into metal capsules to minimize hydration. Sample powder (~20-30 mg) was loaded into gold capsules 10-25 mm in length with an outer diameter (O.D.) of 2.9 mm and an inner diameter (I.D.) of 2.5 mm. The powder was tightly packed using a steel rod. Deionized H_2O (resistivity higher than 180000 Ω·m) was loaded into the capsules using a 1-10 μL micropipette. In IHPV charges, 9-11 wt% H_2O was added to capsules, whereas 3-6 wt% was added to capsules used in hydrated PC runs (Table 2). After loading H_2O and starting material powders, the upper ends of the gold capsules were crimped and then welded shut using a pulsed arc welder while being cooled with wet tissue to avoid heating and thereby H_2O loss from the charge. Following, the gold

capsules were stored in a 120 °C oven overnight, and finally weighed again to check for the presence of leaks. Any sample capsules that deviated by more than 0.0002 g from their after-welding weight were discarded.

2.3.High-temperature, high-pressure experiments

The high-pressure charges were synthetized in the piston cylinders at the Institut des Sciences de la Terre d'Orléans (ISTO), France. Experimental details are provided in Nabyl et al. (2021). We specify that no particular attempt of controlling oxygen fugacity, fO_2, were conducted.

The low-pressure experiments were performed in a vertical internally heated pressure vessel (IHPV) at 800 °C and 200 MPa at ISTO, France, and at 850-1050° C and 800 MPa in a PC press. For the IHPV experiments, the samples were pressurised using pure Ar or Ar-H_2 mixtures (0.15–0.6 MPa H_2 total pressure) in order to vary fO_2 conditions (cf. Scaillet et al., 1992). The more H_2 added, the more reduced, as defined by the water dissociation constant (i.e. $H_2 + ½O_2 = H_2O$, Gaillard et al., 2001). Given that we have loaded high water contents (~9-11 wt%) into the capsules (table 2), and based on the water solubility study of Keppler (2003), we then assumed that the water activity in the charges approached 1 to calculate the redox (fO_2) conditions. The calculated fO_2 values for the IHPV experiments ranged from ~ΔFMQ + 0 to ΔFMQ + 3 (Table 2).

The pressure was monitored by a transducer calibrated against a Heise Bourdon gauge with an accuracy of ± 2 MPa (Gaillard et al., 2001; Andujar et al., 2013). The experiments were performed in double-coiled Kanthal and molybdenum furnaces with near-isothermal conditions (thermal gradient <2–3°C/cm) in the 3 cm-long hotspot (Andujar et al., 2013). Two S-type thermocouples ($Pt_{90}Rh_{10}$/Pt) were placed at the top and bottom of the samples to monitor the temperature with an accuracy of at least ±5 °C (Andujar et al., 2013). In order to ensure the growth of large apatite crystals suitable for major- and trace-element analyses, all experiments were first brought up to1000 °C for 1-3 hours, followed by ramped cooling over 30 minutes to the experimental temperature of 800 °C. For each experiment, 3 to 6 capsules were placed in an aluminium tube fixed at the top of the furnace (hotspot), held by a thin platinum/rhenium wire. To terminate each run, the platinum/rhenium wire was fused

electrically, which dropped the sample container into the cold part of the furnace, ensuring fast isobaric quench (~100 °C/s). After the experiments, capsules were checked for leaks by weighing their mass. Capsules with <0.0002 g weight difference to the pre-experiment weight were considered successful. They were sliced open with a low-speed saw along their length, and half of the run product was mounted in epoxy resin. The sample surface was then polished using ethanol rather than water to limit the dissolution of carbonatite material for optical observation and subsequent analyses.

2.4.Imaging and analytical methods

Run product preparation and all microchemical analyses were performed at the Institut des Sciences de la Terre d'Orléans (ISTO). Back-scattered electron (BSE) images of the run products were taken using a Merlin Compact ZEISS scanning electron microscope (SEM), equipped with a micro-analyser system with a resolution of 129 eV (EDS Bruker-QUANTAX-XFlash6). Energy dispersive spectroscopy (EDS) was carried out to identify the phase assemblages using an accelerating voltage of 15 kV and a working distance of 15 mm.

The major element compositions of apatite and the carbonatite run products were then analysed using a Cameca SXFive electron microprobe equipped with five WDS detectors. All analyses were performed with a 15 kV acceleration voltage, a 10 nA beam current, and a beam size defocused to 10–50 µm, in order to reduce Na-loss during analysis, and to sample the average composition of the quenched carbonatite melts. The following standards were used to calibrate the instrument: albite for Na, apatite for P, orthose for K, calcite for Ca, topaz for F, vanadinite for Cl, MgO for Mg, Al_2O_3 for Al, Fe_2O_3 for Fe, $MnTiO_3$ for Mn and Ti, $SrSO_4$ for S and Sr. Measurement time was 10 s on the peak and 5 s for the background for each element.

The trace element concentrations in apatite and the quenched carbonatite melts were measured by LA-ICP-MS using a RESOlution-SE 193 nm ArF excimer laser with a S155 Laurin Technic sample cell attached to an Agilent 8900 QQQ quadrupole ICP-MS. The laser was operated at a frequency of 5 Hz with energy densities from 2 to about 5 J cm^{-2} on the sample surface. Spot analyses were performed using laser beam diameters of 32-60 µm, depending on the size of the apatite crystals and quench-crystallized melt pools. Measured isotopes were ^{7}Li, ^{23}Na, ^{24}Mg, ^{27}Al, ^{29}Si, ^{39}K, ^{44}Ca,

^{47}Ti, ^{55}Mn, ^{57}Fe, ^{45}Sc, ^{51}V, ^{52}Cr, ^{59}Co, ^{60}Ni, ^{85}Rb, ^{88}Sr, ^{89}Y, ^{90}Zr, ^{93}Nb, ^{95}Mo, ^{133}Cs, ^{137}Ba, ^{139}La, ^{140}Ce, ^{141}Pr, ^{146}Nd, ^{147}Sm, ^{153}Eu, ^{157}Gd, ^{159}Tb, ^{163}Dy, ^{165}Ho, ^{166}Er, ^{169}Tm, ^{172}Yb, ^{175}Lu, ^{178}Hf, ^{181}Ta, ^{182}W, ^{208}Pb, ^{232}Th, and ^{238}U, using dwell times of 10 ms per isotope. Sample measurements were bracketed by analyses of NIST SRM reference glasses to correct for time-dependent drift of sensitivity and mass discrimination. Calibration was conducted using silicate glass standards (NIST SRM 610) with the reference values of Jochum et al. (2011).

Apatite and the quench-crystallized carbonate melt from the piston cylinder samples (Nabyl et al., 2021) were analysed using the same LA-ICP-MS machine as well as an Agilent 7500 CS Quadrupole from the LMV laboratory (Clermont-Ferrand, France) coupled to a 193 nm excimer laser ablation system (frequency of 2 Hz, ablation energy of 1.5 to 3 mJ and beam size of 4 to 33 µm). Concentrations were obtained using the same calibration and methodology (Nabyl et al., 2021). Reference materials NIST 612 and BCR-2G natural basaltic glass were analyzed as secondary standards to ensure the accuracy of the results. The Ca contents of apatite and crystallized melt determined by microprobe were used as the internal standard.

All melt and apatite experimental compositions are available in the supplementary table S1.

2.5.Geochemical criteria for magmatic apatite in carbonatite rocks

More than 7000 apatite compositions from the GEOROC database (https://georoc.eu/) and additional studies were examined (Table S2). The apatite compositions in this database are from 240 localities and 35 countries worldwide. Their compositions reflect a large variety of magmatic, hydrothermal and metamorphic processes and geological environments. These apatites were formed in peralkaline magmatism, carbonatitic magmatism, felsic magmatism, kimberlites, mafic to ultramafic magmatism; we also reported metamorphic, hydrothermal and metasomatic apatites as defined in the source papers. The database also includes apatite compositions from famous REE ore deposits (Bayan Obo, Mountain Pass, and Mount Weld). Based on the source paper interpretations and geochemical modelling of the REE content of apatite in equilibrium with carbonatite melts, 745 natural apatite compositions from carbonatite rocks were identified as being magmatic in origin (see section 4.2.1). For the discussion section of this study, we combined interpretations from source papers with geochemical

modelling to determine the range in composition of magmatic apatite in carbonatite rocks.

3. Experimental Results

All experimental conditions are listed in Table 2, apatite and melt compositions in Table S1, and partition coefficients together with their uncertainties are given in Table 3. In all experiments, the carbonatitic melt quenched to aggregates of sub-micrometer-size elongated crystals (Fig. 2), with larger crystals in hydrous samples (Fig. 2b, c, d). The size of apatite crystals varies from a few tens to a hundred micrometres, with no observed zonation or inclusions (Fig. 2). Apatite crystals have variable morphology, ranging from euhedral or subhedral (Fig. 2a, b, c) to anhedral (Fig. 2d).

Similar to the recent work of Sartori et al. (2023), we used Na-bearing starting materials (Table 1). The melts produced were variably Na-rich and the chemical composition of the run products was homogeneous (Table S1). Equilibrium conditions were obtained between apatite and carbonatite melts at the investigated P-T conditions, as demonstrated by the sharp geometry of the apatite-melt interfaces (Fig. 2), the homogeneity of apatite compositions, and the homogeneous compositions measured in carbonatite melts (Table S1). Partition coefficients were calculated using the Nernst formula as a mass ratio of the element concentration in apatite relative to that in the carbonatite melt: $D_{Element} = C^{Apatite}/C^{Melt}$ (Table 3). The partition coefficients of Sr, Y and REE (D_{REE}) range from 1 to 7 (Fig. 3a). We found that the apatite-melt partition coefficients do not correlate with the volatile contents (H_2O, F, Cl and S) of the carbonatite melt or fO_2 (Table 2, Table 3, Fig. 3). Only two nominally dry experimental charges appear to display D_{REE} slightly lower than the wet ones by ~30 %, but in general, all measured REE partition data are in the range of 1-7 (Table 3) for the large range of Cl, F, S contents and fO_2 conditions explored in our experiments (Table 2). The variations observed for the partitioning of individual REE are within a factor of two for the range of experimental conditions. No clear negative Eu anomalies are observed for reduced or oxidized experiments. We also note that the REE partitioning coefficients determined for the 200 and 800 MPa are indistinguishable.

Accordingly, no clear difference in partition coefficients for Sr, Y and REE (D) is observed between our data and those of Hammouda et al. (2010) or Sartori et al. (2023), despite significant differences in equilibration pressure, temperature, fO_2, halogen and

water contents (Fig. 3-4-5). However, our Sr, Y and REE partition coefficients and those of Hammouda et al. (2010) and Sartori et al. (2023) are much higher than those for the Na- and Si-poor carbonatite experiments of Klemme and Dalpé (2003), and significantly lower than those for apatite-silicate melt partitioning (Waston and Green, 1981; Prowatke and Klemme, 2006) (Fig. 3-4). Figures 4a, b, and c show the partition coefficients of La, Sm and Lu between apatite and melt as a function of SiO_2 concentration in the melt. All published experimental data are shown. For geologically realistic carbonatite systems, i.e. Na-bearing melts with trace amounts of Si, the partition coefficients of all REE are almost constant and lie within the limited range of 1 to 10. We note, however, that the partition coefficients increase dramatically once the melt SiO_2 content exceeds 20 wt%. Most likely, a change must occur in a range of melt SiO_2 contents between 10-30 wt%, where no data exists. This requires further experimental investigations. All in all, these observations allow us to introduce the notion of average partitioning coefficient data for individual RE-elements in carbonatite systems (Table 3), since the carbonatite melts usually have less than 10 wt% SiO_2.

4. Discussion

4.1. Factors controlling the partitioning of REE between apatite and carbonatite melt

Klemme and Dalpé (2003) found that REE were all incompatible in apatite at equilibrium with a Ca-dominated carbonatitic melt at 1 GPa and 1250 °C. Hammouda et al. (2010) found that REE were compatible in apatite in the Si-bearing $CaCO_3$-$Ca_5(PO_4)_3(F,OH)$ system at 4-6 GPa and 1200-1380 °C. Sartori et al. (2023) also showed that REE were all compatible in apatite in the Si-bearing and Na-bearing carbonatite system at 100-200 MPa and 750-1000°C. Similarly, we found that REE are mostly compatible in apatite in Na-bearing systems (Fig. 3). We nevertheless note that in their results, Hammouda et al. (2010) have one datapoint wherein REE appears to be slightly incompatible in apatite (Fig.5). We have recalculated this datapoint from their electron microprobe data, since there is no LA-ICPMS analysis for this experiment. For the sake of transparency in our analysis, we decided to show it, but it is likely that this datapoint is highly uncertain. The detected La content in the carbonatite melt of this experiment is only 0.13 wt%, whereas the other samples of Hammouda et al (2010)

contained wt% of La. A content of 0.13wt% is only two times the average difference between LA-ICPMS and EMP data for the two samples having both types of measurements (and La-contents >1 wt%).

The most commonly considered factors controlling the partition coefficient between a mineral and melt are temperature, pressure, oxygen fugacity, melt and mineral compositions (Blundy and Wood, 2001). Based on the D_{REE} values (Fig. 3) for apatite-melt, there appears to be no clear dependence on temperature, pressure, or oxygen fugacity (Fig. 3; Figure S1). REE partition systematics between apatite and melt can, however, be divided into two subdomains: small ranges of moderate D_{REE} values for carbonatite systems, vs. high and highly variable D_{REE} values for silicate systems (Fig. 4a, b, c). For silicate systems, the inferred apatite substitution mechanism is Si^{4+} + $REE^{3+} = Ca^{2+} + P^{5+}$ (Cherniak, 2000), hereafter the britholite substitution. Klemme and Dalpé (2003) and Hammouda et al. (2010) suggested that this mechanism may also prevail for carbonatite systems. In figure 5a, we plot the DREE versus Si in apatite for the available experimental data. It appears unclear whether silica incorporation in apatite affects DREE. All available data plot in the D_{La} range 1-7 for silica content in apatite varying from 0.2 to 5 wt%, with the exception of the data of Klemme and Dalpé (2003) and one datapoint from Hammouda et al. (2010), ie. the one analyzed by EMPA. These lower values may rather indicate that the substitution mechanism Na^{+} + REE^{3+} = $2Ca^{2+}$ (Cherniak, 2000) is important for apatite in carbonatite systems. Klemme and Dalpé (2003) and Hammouda et al. (2010) worked indeed on Na-free systems. We can thus conclude that in systems containing trace amounts of Si and Na, as expected for natural carbonatite, apatite-melt partitioning data are in the range 1-7.

Figure 5b shows a compilation of natural apatites in a plot REE vs. SiO_2 wt%. The data have been sorted in order to visualize the role of the silica content of the bulk rocks on putative Si-REE substitution in apatites. This is an extension of figure 4 toward natural compositions but it is imperfect, given that the bulk SiO_2 contents of natural carbonated rocks may not represent the silica content of the melt from which the apatites crystallized. Nevertheless, this plot is useful as it shows a clear link between SiO_2 and REE contents in apatites for silica-rich carbonated rocks (SiO_2> 10 wt. %). This relationship is less clear for carbonatite rocks with <10% bulk SiO_2. For most of these low Si-rocks, data are located in a cloud of points at <2 wt% SiO_2 and <2 wt% REE in apatite. The experimental data reported in figure 4 are also plotted in figure 5b. Most

experimental data (Klemme and Dalpé 2003; Hammouda et al., 2010; Sartori et al. 2023; our data) plot in the cloud of points at low SiO_2 contents, where no Si-REE substitution is visible. This is consistent with the D_{REE} data discussed in figure 4 and 5a. Some data by Hammouda et al. (2010), however, plot clearly in the high SiO_2 range and show high REE contents (note that Hammouda et al. 2010 did not measure all REE; ca. 1 wt% might be missing). These data are broadly in the trend indicated by the crystallization of Si-rich carbonatites and consistent with a britholite substitution. Yet, the D_{REE} measured by Hammouda et al. (2010) on high-Si apatites do not significantly differ from others obtained on low-Si ones. This brings us to the surprising conclusion that the britholite substitution does not significantly affect the apatite-melt D_{REE}.

An analysis of the natural and experimental data thus suggests that the partitioning of REE between apatite and carbonatite melt remains in a narrow range for a large set of P-T-fO_2-H_2O-Cl-F-SiO_2-Na_2O conditions expected to prevail in carbonatite systems. REE incorporation in apatite certainly obeys to various substitution mechanisms, involving Si and Na, but more systematic work is needed to clarify this issue. Overall, we use at this stage the average partition coefficient values from this study for each REE in a carbonatite system in the following sections (Table 3).

4.2. Magmatic apatite as a geochemical proxy for carbonatite melt compositions

4.2.1. A geochemical criterion for identifying magmatic apatites

Sartori et al. (2023) suggested that calcite – apatite partitioning of light and heavy REE could be used to distinguish magmatic from hydrothermal phases. Low La/Lu partitioning ratios were shown to reflect hydrothermal signatures. This approach is certainly valid but it requires the analysis of both coexisting phases, an information which is not always available in studies on carbonatites. Here, we propose to use apatite as magmatic proxy and discuss the way to identify such magmatic apatites.

The 745 natural apatites that we selected (red dots in figure 6) have been classified according to the source papers as magmatic apatites formed from carbonatite melts (Table S2). This is mostly based on mineralogical criteria. We further verified their origin by comparing them with calculated compositions of apatite in equilibrium with alkaline and carbonatite melts. Such putative carbonatite melts, resulting from silicate-carbonate immiscibility, are described in Nabyl et al. (2020). They were calculated from

a GEOROC compilation of major and trace element compositions of alkaline melts from the East African rift. These calculated magmatic apatites have Sr concentrations >1000 ppm and a $(La/Yb)_N$ ratios in the range of 20-300 (Fig. 6, see inset on the right for the data distributions and the rectangle marked by the thick dashed red contours). Most red dots in figure 5 match this Sr vs. La/Yb criterion, testifying to their magmatic origin. A majority of blue points (hydrothermal apatite according to the source papers) plots below the La/Yb threshold of 20. Lower La/Yb ratios are expected for secondary apatite crystallized from fluids since La is more fluid mobile than Yb. We however recognize that a significant number of blue dots, categorized by the authors as hydrothermal, plots above La/Yb=20, where equilibrium magmatic apatite should form in such systems. Those cases were probably only moderately affected by metasomatic events and/or preserved a geochemical signature intermediate between magmatic and hydrothermal, possibly involving hydrosaline brine (e.g. Yuan et al., 2023; Walter et al., 2021). Finally, we underline that the Sr-La/Yb data for natural apatite found in carbonatites (red dots) and those found in alkaline melt (red area with dashed grey contours in fig.6) are indistinguishable, suggesting an overwhelming genetic link between these magmas, that is to say, an equilibration by silicate-carbonate immiscibility.

4.2.2. Range of REE-contents in carbonatite melts from apatites

Using the D_{REE} averages (and standard deviations) in Table 3 and the magmatic apatite compositions (red dots in figure 6), we calculated the REE contents of the coexisting carbonatite melts. The REE contents of the selected apatites are shown in Fig. 7a, and the calculated REE contents of the equilibrated carbonatite melts are shown in Fig. 7b. The calculated REE abundances of the carbonatite melts show marked variation, covering more nearly three orders of magnitude, i.e., ranging from ~100 ppm to >10,000 ppm for La normalized to chondrites. This defines the REE content of carbonatite melts in equilibrium with apatite. These are probably not primary carbonatite liquids, but they define the REE contents of the melt when apatite saturation was reached.

As a sensitivity test, we modelled the effect of crystallization on the REE contents of the carbonatite melts. We considered the crystallization of both calcite and apatite, because of their abundance in carbonatite rocks (Chakhmouradian et al., 2017;

Anenburg et al., 2020; Mollé et al., 2021; Sartori et al., 2023; Yaxley et al. 2022; Weindendorfer et al., 2017). Figure 7b shows the effect of 50% calcite crystallization and 30% apatite crystallization modelled by the partition coefficients in Mollé et al. (2021) and this study. The red and the green arrows indicate the changes in REE contents in response to fractionation of apatite and calcite, respectively. One can see that both crystallization processes have a moderate effect on the melt REE contents (Fig. 7b). In detail, we note that apatite crystallization tends to deplete the carbonatite melts in REE, but we do not expect more than 30 wt% apatite crystallization from such melts. Therefore, the more than two orders of magnitude variation recorded by apatite compositions and the inferred co-existing melts cannot be attributed to crystal fractionation. The large variation in REE contents we see in Fig. 7b must be an original feature of the carbonatite melts that can only be moderately affected by fractionation. Hereafter, we show how the genesis of carbonatite melts can be interpreted using the REE contents found in apatite.

4.3. Capturing the origin of carbonatite melts by means of their REE contents

Petrological constraints indicate that mantle carbonatite melts are unlikely to reach the surface (Yaxley et al., 2021), making the assessment of their REE contents difficult. Coltorti et al. (1999), who reconstructed mantle carbonatite REE contents using metasomatized peridotites, suggested that carbonatite melts have low to intermediate REE contents with e.g., La in the range of ~500 to 1000 normalized to chondrite. We note that the inferred REE pattern for the mantle carbonatite melt is flatter than that of the calculated melt compositions involving apatite (light brown field in Fig. 7b). More recently, O'Reilly and Griffin (2000) defined the REE contents of mantle apatites, which could directly be used here. However, it is unclear whether normalized or unnormalized REE data are reported in their tables, regretfully rendering the use of these data impracticable. Although we acknowledge that the REE-content range of mantle carbonatites is poorly constrained, we suggest that the range of REE contents shown in figure 7b is unlikely to be solely inherited from mantle partial melting. Instead, we consider that other geological processes, i.e. liquid immiscibility, may cause the diverse REE pattern of carbonatite melts in figure 7b.

Figure 7c shows the calculated REE contents for carbonatite melts produced by immiscibility with strongly peralkaline silicate melts from the East African Rift (Nabyl

et al., 2020). The lowest REE contents correspond to carbonatite melts produced from melilitic/nephelenitic melts, whereas the highest REE contents correspond to carbonatite melts produced from phonolitic melts (Nabyl et al., 2020). The range of REE contents determined for these melts almost perfectly matches the melt compositions calculated using the apatite proxy (Fig. 7b, c). For both melt compositions, i.e. calculated from apatite or from immiscibility, the lowermost values for La, Sm and Lu normalized to chondrite are ca. 100, 40 and 5, respectively. The high range for La, Sm and Lu recorded by our apatite proxy (Fig. 7b) is somewhat lower than that of the carbonatite melts produced by immiscibility from phonolitic melts (Fig. 7c). This may be due to the fact that very REE-rich carbonatite melts are not systematically apatite saturated (see Mollé et al., 2021). We thus suggest that the REE contents of carbonatite melts as reconstructed using the apatite proxy are mostly consistent with their genesis by liquid immiscibility from peralkaline melts. This is also consistent with the fact that the Sr contents and the $(La/Yb)_N$ ratios of magmatic apatites in equilibrium with silica-undersaturated peralkaline and carbonatite melts are indistinguishable (Fig. 6). The variation in REE contents of carbonatite melts thus largely reflects the level of differentiation of the parental peralkaline melts as suggested by Nabyl et al. (2020).

4.4. Comparison with carbonatite rocks and ore deposits

The REE contents of more than 3500 natural carbonate rocks from the GEOROC database are plotted in Fig. 1. The range of REE contents of the carbonate rocks from various geological settings (rift volcanoes, intraplate volcanoes, ocean islands, continental flood basalts and Archean cratons) show a similar variability to the carbonatite melt compositions predicted by the apatite proxy (Fig. 7b) and by immiscibility from strongly peralkaline melts (Fig. 7c). The lowest REE contents in carbonatite rocks (Fig.1) are indistinguishable from the lowest REE contents in inferred carbonatite melts (Fig. 7b, c). The upper range of REE contents in the natural carbonatite rocks (Fig. 1) is somewhat higher than the most REE-rich melts produced by immiscibility from phonolitic melts, which could reflect fluid-related processes (Anenburg et al., 2020; Louvel et al., 2022) or the fact that the most REE-rich carbonated melts are not saturated in apatite (Mollé et al., 2021).

5. Conclusion

Our experimental calibration of the apatite-carbonatite partitioning shows that apatite found in carbonatite rocks can be used as a proxy to constraint the composition of the poorly defined carbonatite melts. This apatite proxy allows us to see through magmatic crystallization and subsolidus metasomatic interactions. Our study reveals that carbonatite melts display a large range of REE contents that can be linked to the significant variations found in the REE contents of carbonatite rocks, including some REE deposits. Our analysis indicates that carbonatite melts crystallizing apatites are REE-rich (>10,000 ppm) to REE-poor (~100 ppm), which seemingly reflects immiscibility at various differentiation stages. While subsolidus fluid-rock interactions unquestionabl affect and redistribute REE between minerals of carbonatites, we suggest that the bulk rock REE contents are primarily controlled by magmatic processes.

Acknowledgments

We gratefully acknowledge the constructive comments of journal editor Dr Rosemary Hickey-Vargas and two anonymous reviewers. This study was financially supported by the ANR LabEx VOLTAIRE (LABX-100-01), the ANR GASTON (ANR-18-CE31-0021) and the EquipEx PLANEX (ANR-11-EQPX-0036). National Natural Science Foundation of China (42373038, 42225202, 42073004, 42073007), Fundamental Research Funds for the Central Universities, China University of Geosciences (Wuhan) G1323523034, CUG230610, provided supports to H.G. during revision of this manuscript.

References

Anenburg, M., Broom-Fendley, S. and Chen, W. (2021) Formation of Rare Earth Deposits in Carbonatites. Elements 17, 327-332.

513 Anenburg, M., Mavrogenes, J.A., Frigo, C., Wall, F. (2020) Rare earth element
514 mobility in and around carbonatites controlled by sodium, potassium, and silica. *Sci*
515 *Adv* 6, eabb6570.

516 Berkesi, M., Bali, E., Bodnar, R.J., Szabó, Á., Guzmics, T. (2020) Carbonatite and
517 highly peralkaline nephelinite melts from Oldoinyo Lengai Volcano, Tanzania: The
518 role of natrite-normative fluid degassing. *Gondwana Research* 85, 76-83.

519 Chakhmouradian, A.R., Reguir, E.P., Zaitsev, A.N., Couëslan, C., Xu, C., Kynický, J.,
520 Mumin, A.H., Yang, P. (2017) Apatite in carbonatitic rocks: Compositional variation,
521 zoning, element partitioning and petrogenetic significance. *Lithos* 274-275, 188-213.

522 Cherniak, D. (2000) Rare earth element diffusion in apatite. *Geochimica et*
523 *Cosmochimica Acta* 64, 3871-3885.

524 Coltorti, M., Bonadiman, C., Hinton, R., Siena, F., Upton, B. (1999) Carbonatite
525 metasomatism of the oceanic upper mantle: evidence from clinopyroxenes and glasses
526 in ultramafic xenoliths of Grande Comore, Indian Ocean. *Journal of Petrology* 40, 133-
527 165.

528 Dasgupta R. (2013) Ingassing, Storage, and Outgassing of Terrestrial Carbon through
529 Geologic Time. *Reviews in Mineralogy and Geochemistry* 75 (1): 183–229. doi:
530 https://doi.org/10.2138/rmg

531 de Moor, J.M., Fischer, T.P., King, P.L., Botcharnikov, R.E., Hervig, R.L., Hilton, D.R.,
532 Barry, P.H., Mangasini, F., Ramirez, C. (2013) Volatile-rich silicate melts from
533 Oldoinyo Lengai volcano (Tanzania): Implications for carbonatite genesis and eruptive
534 behavior. *Earth and Planetary Science Letters* 361, 379-390.

535 Foley, S.F., Yaxley, G.M., Rosenthal, A., Buhre, S., Kiseeva, E.S., Rapp, R.P., Jacob,
536 D.E. (2009) The composition of near-solidus melts of peridotite in the presence of CO2
537 and H_2O between 40 and 60 kbar. *Lithos* 112, 274-283.

538 Gittins, J. and Mitchell, R.H.J.G.M. (2023) The genesis of calcite and dolomite
539 carbonatite-forming magma by liquid immiscibility: a critical appraisal. 160, 1463-
540 1480.

Guzmics, T., Berkesi, M., Bodnar, R.J., Fall, A., Bali, E., Milke, R., Vetlényi, E., Szabó, C. (2019) Natrocarbonatites: A hidden product of three-phase immiscibility. *Geology* 47, 527-530.

Guzmics, T., Mitchell, R.H., Szabó, C., Berkesi, M., Milke, R., Ratter, K. (2012) Liquid immiscibility between silicate, carbonate and sulfide melts in melt inclusions hosted in co-precipitated minerals from Kerimasi volcano (Tanzania): evolution of carbonated nephelinitic magma. *Contributions to Mineralogy and Petrology* 164, 101-122.

Guzmics, T., Zajacz, Z., Mitchell, R.H., Szabó, C., Wälle, M. (2015) The role of liquid–liquid immiscibility and crystal fractionation in the genesis of carbonatite magmas: insights from Kerimasi melt inclusions. *Contributions to Mineralogy and Petrology* 169, 1-18.

Halama, R., Vennemann, T., Siebel, W., Markl, G. (2005) The Grønnedal-Ika carbonatite–syenite complex, South Greenland: carbonatite formation by liquid immiscibility. *Journal of Petrology* 46, 191-217.

Hammouda, T., Chantel, J., Devidal, J.-L. (2010) Apatite solubility in carbonatitic liquids and trace element partitioning between apatite and carbonatite at high pressure. *Geochimica et Cosmochimica Acta* 74, 7220-7235.

Keppler, H. (2003) Water solubility in carbonatite melts. American Mineralogist 88, 1822-1824.

Klemme, S., Dalpé, C. (2003) Trace-element partitioning between apatite and carbonatite melt. *American Mineralogist* 88, 639-646.

Le Bas, M. (1989) Diversification of carbonatite. In: Bell, K. (Ed.), *Carbonatites, Genesis and Evolution*, 428-445.

Lee, W.-jJ., Wyllie, P.J. (1994) Experimental data bearing on liquid immiscibility, crystal fractionation, and the origin of calciocarbonatites and natrocarbonatites. *International Geology Review* 36, 797-819.

Louvel, M., Etschmann, B., Guan, Q. *et al.* Carbonate complexation enhances hydrothermal transport of rare earth elements in alkaline fluids. *Nat Commun* **13**, 1456 (2022). https://doi.org/10.1038/s41467-022-28943-z

570 Massuyeau M., et al. (2020) MAGLAB: A computing platform connecting geophysical
571 signatures to melting processes in Earth's mantle. *Physics of the Earth and Planetary*
572 *Interiors*, pp.106638. ⟨10.1016/j.pepi.2020.106638⟩.

573 McLemore, V. (2018) Rare Earth Elements (REE) Deposits Associated with Great
574 Plain Margin Deposits (Alkaline-Related), Southwestern United States and Eastern
575 Mexico. *Resources* 7, 44 p.

576 Mitchell, R.H. (2009) Peralkaline nephelinite–natrocarbonatite immiscibility and
577 carbonatite assimilation at Oldoinyo Lengai, Tanzania. *Contributions to Mineralogy*
578 *and Petrology* 158, 589-598.

579 Mollé, V., Gaillard, F., Nabyl, Z., Tuduri, J., Di Carlo, I., Erdmann, S. (2021)
580 Crystallisation sequence of a REE-rich carbonate melt: an experimental approach.
581 *Comptes Rendus. Géoscience* 353, 217-231.

582 Nabyl, Z., Gaillard, F., Tuduri, J., Di Carlo, I. (2021) No direct effect of F, Cl and P on
583 REE partitioning between carbonate and alkaline silicate melts. *Comptes Rendus.*
584 *Géoscience* 353, 233-272.

585 Nabyl, Z., Massuyeau, M., Gaillard, F., Tuduri, J., Iacono-Marziano, G., Rogerie, G.,
586 Le Trong, E., Di Carlo, I., Melleton, J., Bailly, L. (2020) A window in the course of
587 alkaline magma differentiation conducive to immiscible REE-rich carbonatites.
588 *Geochimica et Cosmochimica Acta* 282, 297-323.

589 O'Reilly, Suzanne & Griffin, W. (2000). Apatite in the mantle: Implications for
590 metasomatic processes and high heat production in Phanerozoic mantle. Lithos. 53.
591 217-232. 10.1016/S0024-4937(00)00026-8.

592 Prowatke, S., Klemme, S. (2006) Trace element partitioning between apatite and
593 silicate melts. *Geochimica et Cosmochimica Acta* 70, 4513-4527.

594 Sartori, G., Galli, A., Weidendorfer, D. and Schmidt, M.W. (2023) A tool to distinguish
595 magmatic from secondarily recrystallized carbonatites—Calcite/apatite rare earth
596 element partitioning. *Geology* 51, 54-58.

597 Scaillet, B., Pichavant, M., Roux, J., Humbert, G. and Lefevre, A. (1992) Improvements
598 of the Shaw membrane technique for measurement and control of fH_2 at high
599 temperatures and pressures. *American Mineralogist* 77, 647-655.

Sweeney, R.J. (1994) Carbonatite melt compositions in the Earth's mantle. *Earth and Planetary Science Letters* 128, 259-270.

Veksler, I., Nielsen, T., Sokolov, S. (1998) Mineralogy of crystallized melt inclusions from Gardiner and Kovdor ultramafic alkaline complexes: implications for carbonatite genesis. *Journal of Petrology* 39, 2015-2031.

Verplanck, P.L., Mariano, A.N., Mariano, A.J. (2016) Rare earth element ore geology of carbonatites, in: Verplanck, P.L., Hitzman, M.W. (Eds.), Rare earth and critical elements in ore deposits. Society of Economic Geologists, Inc, Littleton, CO, USA, pp. 5-32.

Walter, B. F., Giebel, R. J., Steele-MacInnis, M., Marks, M. A., Kolb, J., & Markl, G. (2021). Fluids associated with carbonatitic magmatism: a critical review and implications for carbonatite magma ascent. Earth-Science Reviews, 215, 103509. https://doi.org/10.1016/j.earscirev.2021.103509

Watson, E.B., Green, T.H. (1981) Apatite/liquid partition coefficients for the rare earth elements and strontium. *Earth and Planetary Science Letters* 56, 405-421.

Weidendorfer, D., Schmidt, M.W., Mattsson, H.B. (2017) A common origin of carbonatite magmas. *Geology* 45, 507-510.

Wood, B.J., Blundy, J.D. (2014) 3.11 - Trace Element Partitioning: The Influences of Ionic Radius, Cation Charge, Pressure, and Temperature. In: Holland, H.D. and Turekian, K.K. Eds.), *Treatise on Geochemistry (Second Edition)*. Elsevier, Oxford, 421-448.

Xu, C., Campbell, I.H., Allen, C.M., Huang, Z., Qi, L., Zhang, H., Zhang, G. (2007) Flat rare earth element patterns as an indicator of cumulate processes in the Lesser Qinling carbonatites, China. *Lithos* 95, 267-278.

Yaxley, G.M., Anenburg, M., Tappe, S., Decree, S., Guzmics, T. (2022) Carbonatites: Classification, Sources, Evolution, and Emplacement. *Annual Review of Earth and Planetary Sciences* 50, 261-293.

Yaxley, G.M., Kjarsgaard, B.A., Jaques, A.L. (2021) Evolution of Carbonatite Magmas in the Upper Mantle and Crust. *Elements: An International Magazine of Mineralogy, Geochemistry, and Petrology* 17, 315-320.

630 Yuan X. et al. (2023) Transition from carbonatitic magmas to hydrothermal brines:
631 Continuous dilution or fluid exsolution?.*Sci. Adv.***9**, eadh0458.
632 DOI:10.1126/sciadv.adh0458

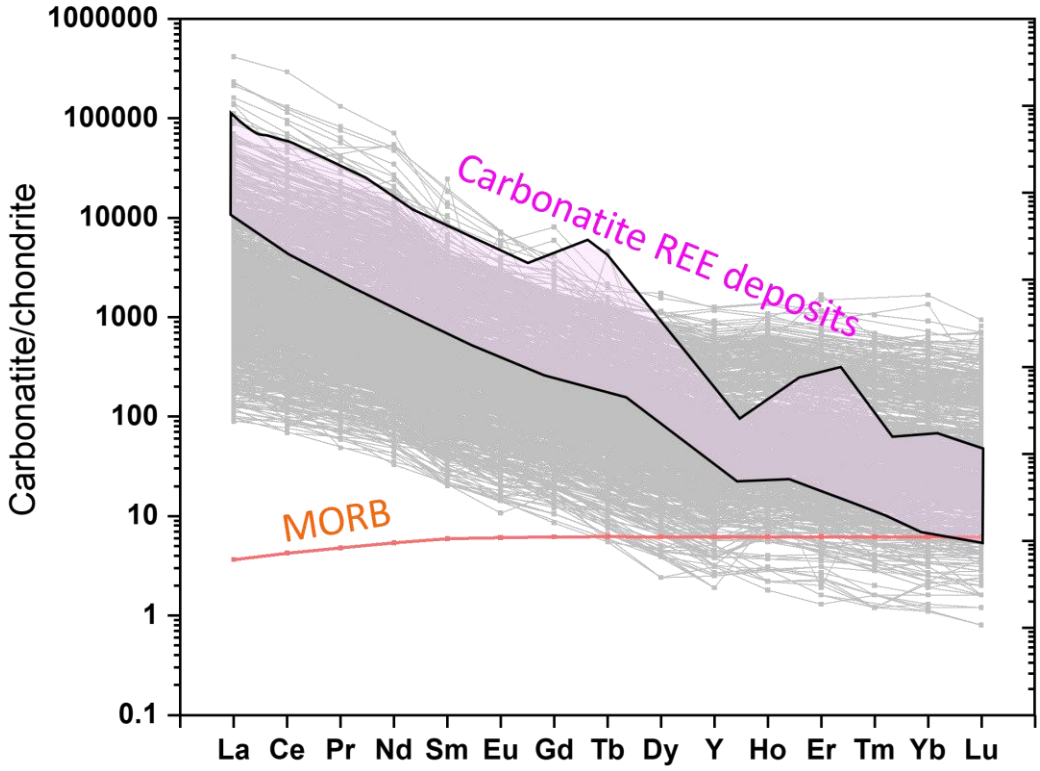

633

634 Fig. 1. REE contents of carbonatite rocks (more than 3500 natural magmatic carbonatite
635 rocks from the GEOROC database; http://georoc.mpch-mainz.gwdg.de/georoc/)
636 normalised to the chondrite composition of McDonough and Sun (1995). The pink
637 pattern represents the compositional range of carbonatite REE deposits including Bayan
638 Obo, Mianing deposits and Mountain Pass (Verplanck et al., 2016).

639

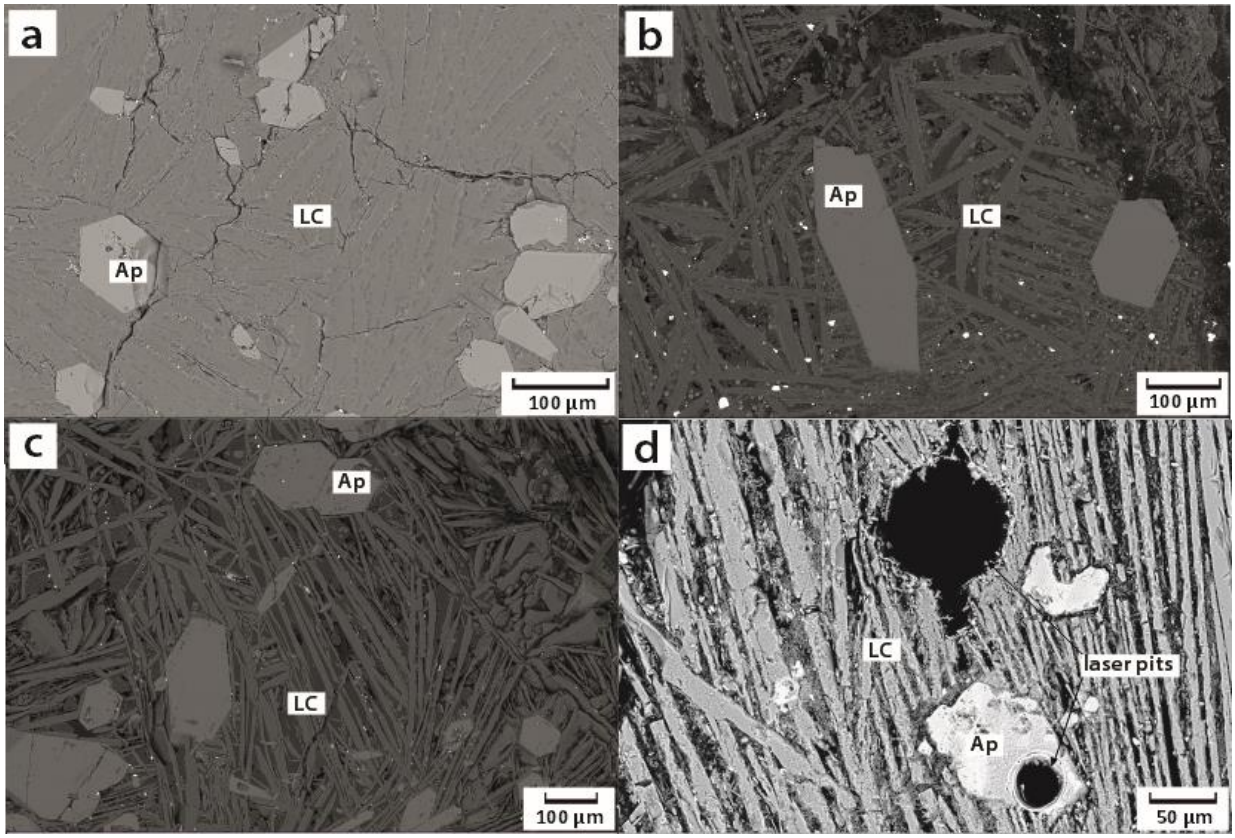

640

641 Fig. 2. Back-scattered electron images of experimental run products. The carbonatitic
642 melt quenched as aggregates of sub-micrometer-size elongated crystals, with larger
643 apatite crystals in hydrous samples. (a) HGAP11 (carbonate + apatite); (b) HGAP08
644 (carbonate + apatite + H_2O + NaF); (c) HGAP12 (carbonate + apatite + H_2O); (d)
645 HGAP17 (carbonate + apatite + H_2O) with laser pits in the apatite and quenched melt.
646 Ap-apatite; LC-carbonatite melt. For details on the experiments, please see Table 1.

647

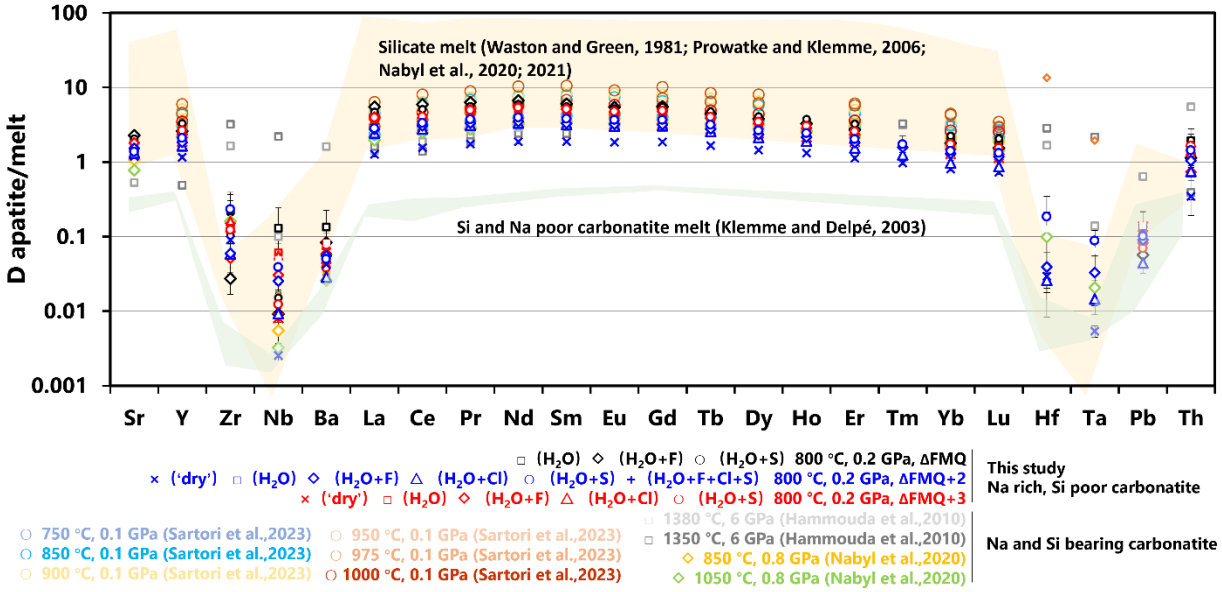

Fig. 3. Experimentally determined partition coefficients for apatite and melt from this study and previous studies (Waston and Green, 1981; Klemme and Daple, 2003; Prowatke and Klemme, 2006; Hammouda et al., 2010; Nabyl et al., 2020; 2021). Apatite-melt partition coefficients for Na- and Si-bearing carbonatite melts (individual data points, see legend for details) fall between those of Si- and Na-poor carbonatite melts (indicated by the green compositional field) and silicate melt (indicated by the yellow compositional field).

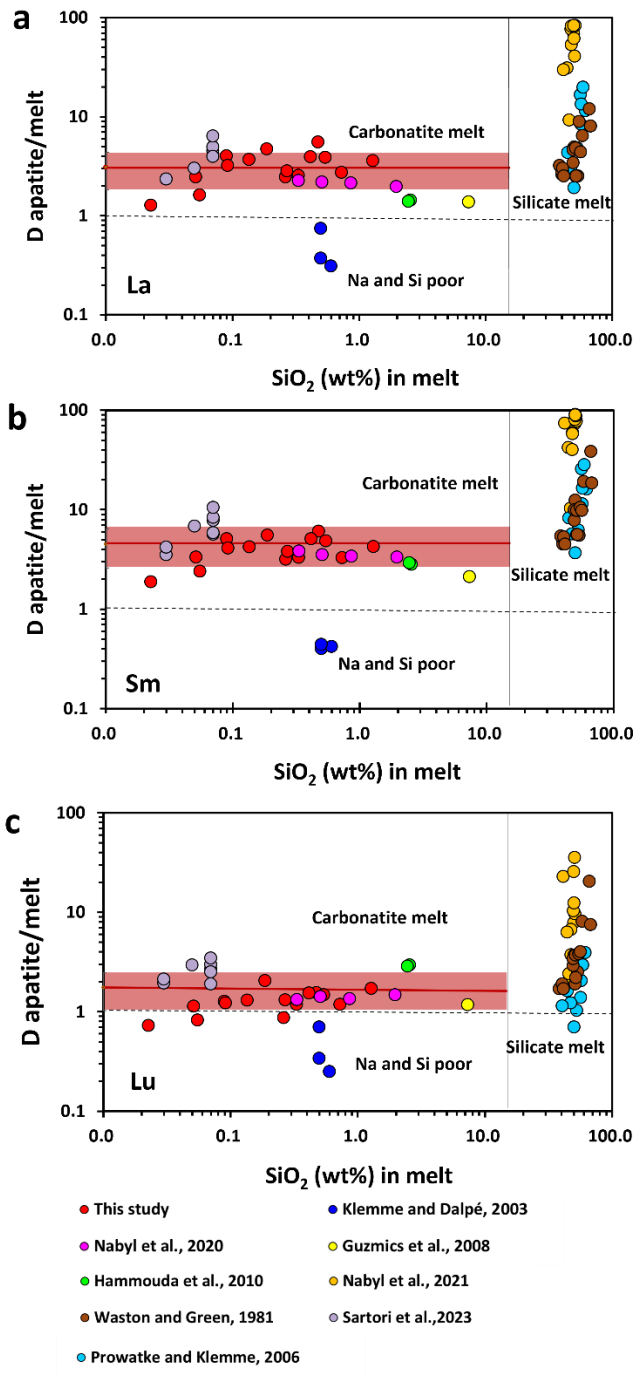

660

661 Fig. 4. Partition coefficients for La, Sm and Lu between apatite and melt as a function
662 of SiO_2 concentration in the melt. The horizontal red lines represent the average
663 partition coefficients between apatite and carbonatite melt, and the red fields represent
664 1 sigma standard deviations of the average partition coefficients. Note that the data from
665 Klemme and Dalpé (2003) below the dashed black unit lines are not included in the
666 average calculations, because the Na and Si poor experimental carbonatite
667 compositions are not geologically realistic compositions.

668

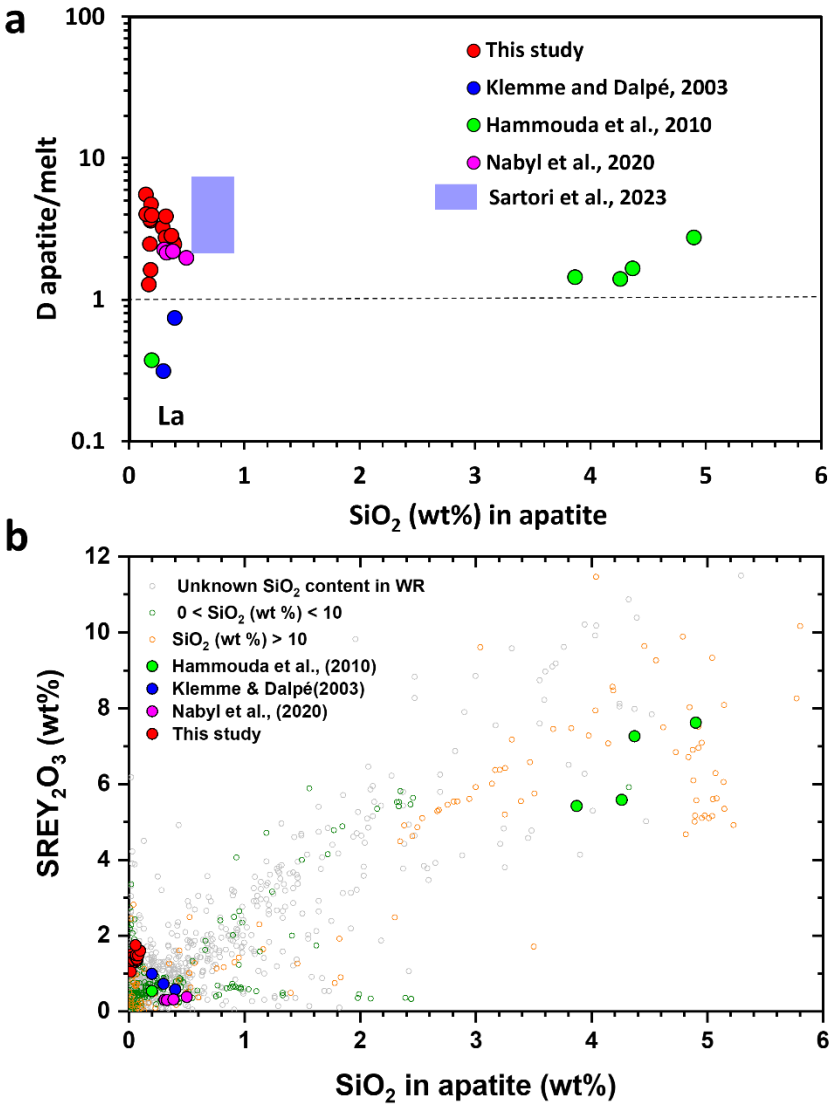

669

670 Fig. 5. (a) Partition coefficients for La between apatite and melt as a function of SiO_2
671 concentration in apatite. (b) $SREY_2O_3$ (total of REE and Y) content (wt%) vs. SiO_2
672 content (wt%) in natural apatite. The color circles represent the experimental data. The
673 natural apatite data are for whole-rock compositions (WR) with unknown SiO_2 content,
674 SiO_2 in WR <10 wt%, and SiO_2 in WR >10% wt%.

675

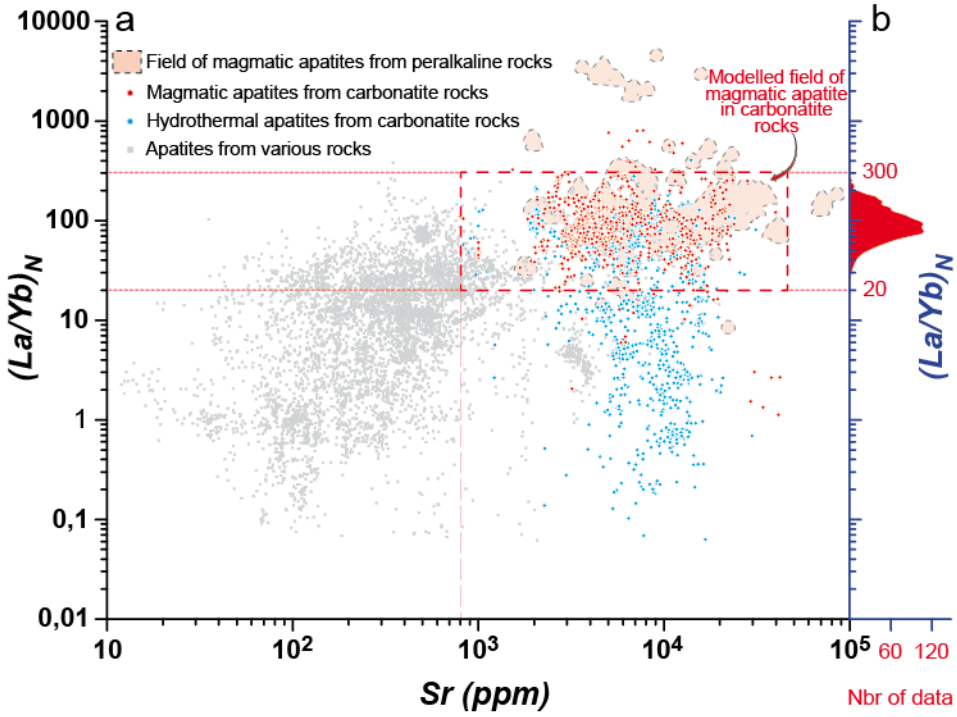

676

677

678 Fig. 6. (a) Sr concentrations vs. $(La/Yb)_N$ ratios in apatite from various geological
679 environments. The $(La/Yb)_N$ ratios are values normalised to the chondrite composition
680 of McDonough and Sun (1995). All data are from the GEOROCK database and
681 additional literature in supplementary materials. Magmatic apatite in carbonatites has
682 relatively high $(La/Yb)_N$ values and Sr concentrations. (b) Calculated $(La/Yb)_N$ ratios
683 for apatite crystals in equilibrium with silica-undersaturated peralkaline and carbonatite
684 immiscible melts (see Nabyl et al 2020 for the source data); number of data for
685 magmatic apatite in carbonatite rocks.

686

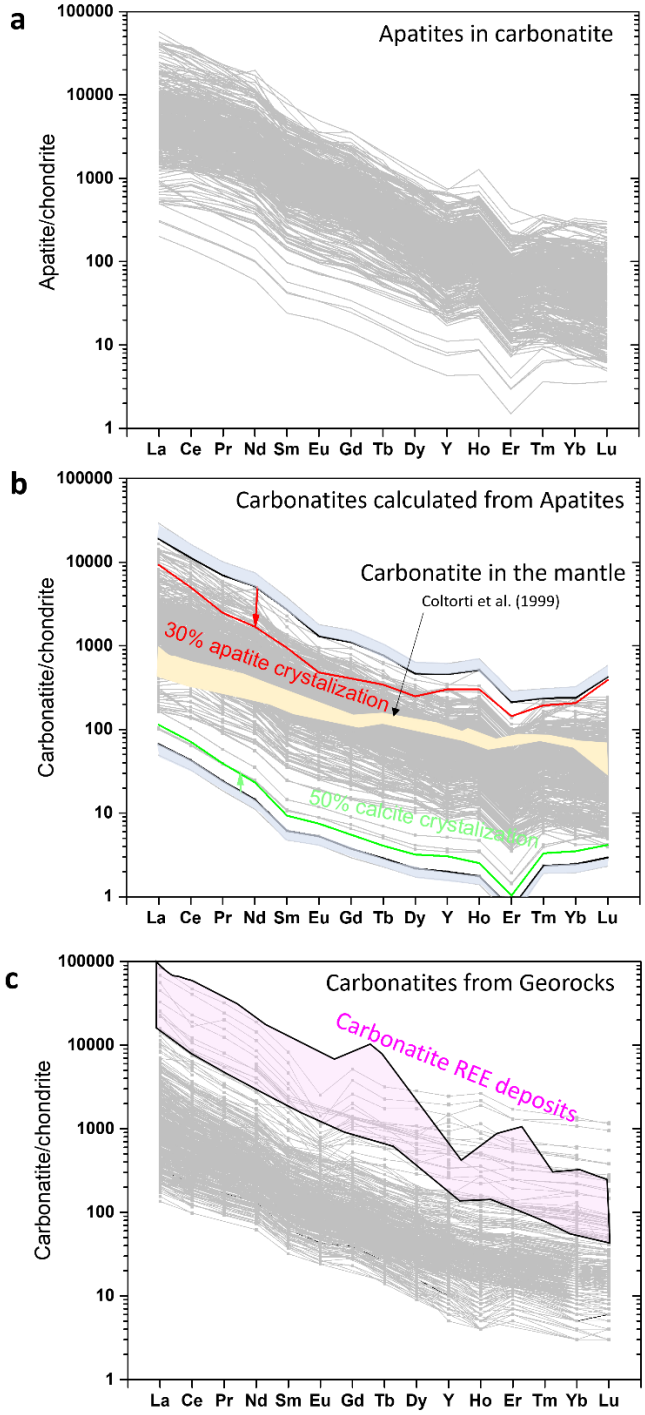

687

688 Fig. 7. REE contents of apatites and carbonatite melts normalised to the chondrite
689 composition of McDonough and Sun (1995). (a) REE contents of 745 magmatic
690 apatites identified as magmatic in origin. (b) REE contents of carbonatite melts were
691 calculated from the magmatic apatite compositions; blue areas show the compositions
692 with consideration of Ds (partition coefficients between apatite and carbonatite melts)

with 1 sigma standard deviation; green and red broken lines, respectively, show the effects of calcite and apatite crystallization on the REE abundance of carbonatite melts calculated assuming equilibrium fractionation. The yellow field is the composition of carbonatite in the mantle obtained from Coltorti et al. (1999). (c) REE contents of carbonatites calculated as immiscible melts in equilibrium with mafic to felsic alkaline melt compositions (data after Nabyl et al., 2020). The pink field represents the compositions of carbonatite REE deposits including Bayan Obo, Mianing deposits and Mountain Pass (Verplanck et al., 2016).